Tuning the atomic and electronic structures of mirror twin boundaries in molecular beam epitaxy grown $MoSe_2$ monolayers via rhenium doping

Zhoubin Yu[1, 4†], Yipu Xia[2†], Hannu-Pekka Komsa[3*], Junqiu Zhang[2], Maohai Xie[2*], and Chuanhong Jin[1, 4, 5*]

[1] State Key Laboratory for Silicon and Advanced Semiconductor Materials, School of Materials Science and Engineering, Zhejiang University, Hangzhou, Zhejiang 310024, China
[2] Physics Department, The University of Hong Kong, Pokfulam Road, Hong Kong, China
[3] Microelectronics Research Unit, University of Oulu, 90014 Oulu, Finland
[4] Jihua Laboratory, Foshan, Guangdong 528200, China
[5] Shanxi-Zheda Institute of Advanced Materials and Chemical Engineering, Taiyuan 030000, China
[†] These authors contribute equally to this work.
[*] Corresponding author

E-mail: Hannu-Pekka.Komsa@oulu.fi, mhxie@hku.hk, chhjin@zju.edu.cn

Received xxxxxx
Accepted for publication xxxxxx
Published xxxxxx

Abstract

Interplay between defects like mirror twin boundaries (MTBs) and dopants may provide additional opportunities for furthering the research on two-dimensional monolayer (ML) transition metal dichalcogenides (TMDs). In this work, we successfully dope rhenium (Re) into molecular beam epitaxy grown ML $MoSe_2$ and confirm the formation of a new type of MTBs, named 4|4E-M (M represents metal, Mo/Re) according to the configuration. Data from statistic atomic resolution scanning transmission electron microscopy (STEM) also reveals a preferable MTB enrichment of Re dopants, rather than intra-domain. In conjunction with density functional theory calculation results, we propose the possible routes for Re doping induced formation of 4|4E-M MTBs. Electronic structures of Re doped MTBs in ML $MoSe_2$ are also predicted theoretically and then preliminarily tested by scanning tunnelling microscopy and spectroscopy.

Keywords: 2D Materials, Transition Metal Dichalcogenide, Doping, Mirror Twin Grain Boundary

1. Introduction

Monolayer (ML) transition metal dichalcogenides (TMDs) MX_2 (M for transition metals, X for chalcogens), as an important family of two-dimensional (2D) materials, hold promise for potential applications in nanoelectronics[1], optoelectronics[2], and catalysis[3]. Given that defects play a more prominent role in 2D materials compared to their bulk counterparts, the investigation of defects in 2D TMDs has garnered increasing attention, resulting in a considerable body of research[4–7].

Defects can be categorized into two primary categories based on their origins: intrinsic defects, such as vacancies[8,9] and grain boundaries[10,11], and extrinsic defects like

dopants[12,13]. Of them, vacancy is a frequently observed intrinsic defect in 2D TMDs due to its formation energy, which could compromise the 2D TMD devices performance such as the lowering of carrier mobility[14]. On the other side, vacancies also hold potential advantages, like sulphur vacancies in MoS_2 serving as active centres for high efficient CO_2 hydrogenation[15]. Incorporation of extrinsic dopants, has been widely utilized to modulate the electronic structures and chem-physical properties of 2D TMDs[16–19]. Depending on valance electron characteristics, dopants can be either isoelectronic or non-isoelectronic. Isoelectronic doping like the inter-substitution between transition metal element (such as Mo and W) and chalcogen (S, Se, and Te) has been successful through the full concentration range, which allowed for a wide tuning of 2D TMD band gaps[20,21]. Non-isoelectronic doping in 2D TMDs has been typically realized by substituting metal element (Mo/W) in group VI TMDs with group V (like V, Nb)[22–24] and group VII (like Mn, Re)[25–27] metals. Thus, due to their distinct valence electrons, electronic doping (e.g. Re as the acceptor, and Nb as the donor) and atomic defects and novel phases are introduced into the host 2D TMDs[24,28]. For example, Re doping into ML MoS_2 could drive a H-to-T' phase transition due to the above-threshold level injection of extra electrons[13,29].

Mirror twin boundaries (MTBs), also denoted as inversion domain boundaries, are recognized as one of the most intriguing line defects in 2D TMDs for their physical properties[30] such as charge density waves (CDW)[31,32], and Tomonaga-Luttinger liquid (TLL)[33,34] and other one-dimensional (1D) physics[34]. Of particular interest is the ability to adjust the MTB in terms of density, structure and composition. In this regard, Coelho et al.[35] achieved MTB formation by post deposition of Mo and Ti onto annealed $MoSe_2$ and $MoTe_2$. Similarly, Wang et al.[24] and Pathirage et al.[36] introduced Nb and V doping into WSe_2, a material not predisposed to MTB formation, yet still resulting in high density of MTBs. Moreover, in Nb doped WSe_2[24] and our previously reported Re doped $MoSe_2$[37], a novel MTB configuration emerged along the metal zigzag (M-zz) direction, distinct from the previously reported chalcogen zigzag (X-zz) orientation[4,38].

Co-introduction of MTBs and dopants into 2D TMDs and the associated research remain sacrificed. Interplays between MTBs and dopants may provide further opportunities to tune the electronic structures of the MTBs and the host 2D TMDs. For example, the charge transfer from Re dopants to the 1D metallic MTBs may further boost the electron-electron interactions in MTBs, a desirable feature for 1D physics.

Molecular beam epitaxy (MBE) has proven effective in fabricating 2D TMDs with high-density MTBs[39,40]. Thus, we employ MBE to prepare Re doped $MoSe_2$ samples to delve deeper into the characteristics of this newly identified MTB configuration. Utilizing techniques such as atomic resolution scanning transmission electron microscopy (STEM), density functional theory (DFT), and scanning tunnelling microscopy/spectroscopy (STM/S), we elucidate the process of MTB formation and its impact on electronic structure following Re doping.

2. Materials and methods

2.1 Sample Preparation

Three sets of samples were prepared by MBE on highly oriented pyrolytic graphite (HOPG) substrates, primarily differing in the concentration of Re doping, i.e., undoped, lightly Re doped, and heavily Re doped $MoSe_2$ as a comparison. Pristine undoped $MoSe_2$ ML was grown at a substrate temperature of ~400°C with Mo and Se fluxes (flux ratio Mo/Se ~ 1/10) applied to the substrate at the same time, and the sample was later annealed at ~500°C without Se irradiation. For the lightly doped sample, $MoSe_2$ was initially grown following the above standard procedure, then the sample was annealed at ~600°C without Se irradiation to reduce the density of MTBs[37,41]. Subsequently, the Re source was applied for 1 minute and incorporated into the $MoSe_2$. In the case of the heavily doped sample, after the standard growth and annealing procedure of $MoSe_2$ the Re and Se sources were applied for 40 minutes at a substrate temperature of ~300°C to dope Re atoms into $MoSe_2$ as well as to grow $ReSe_2$-$MoSe_2$ heterostructure. Finally, all sources were closed to complete the growth process.

2.2 ADF-STEM characterization

As grown Re doped $MoSe_2$ films on HOPG were transferred onto copper based lacey carbon film TEM grids via the micromechanical exfoliation using paraffin wax as the coating and protection layer. To achieve a clean sample, the paraffin wax coated sample was washed with acetone repeatedly. Atomic resolution annular dark field STEM (ADF-STEM) was performed in a probe-side spherical aberration corrected STEM (Thermofisher Titan Chemi STEM). This microscope was operated at an acceleration voltage of 200 kV, a convergence angle of 30 mrad, and a collection angle of 53-200 mrad, respectively.

2.3 STM/S Characterization

STM/S measurements were carried out in a Unisoku USM 1500 STM at 77K. A constant-current mode with the tunnelling current of 100 pA was applied for the STM measurements. Tungsten tips were calibrated on clean Ag(111) surface before scanning the samples.

2.4 DFT calculations

All calculations were carried out with the Vienna *Ab-initio* Simulation Package (VASP) using the Perdew-Burke-

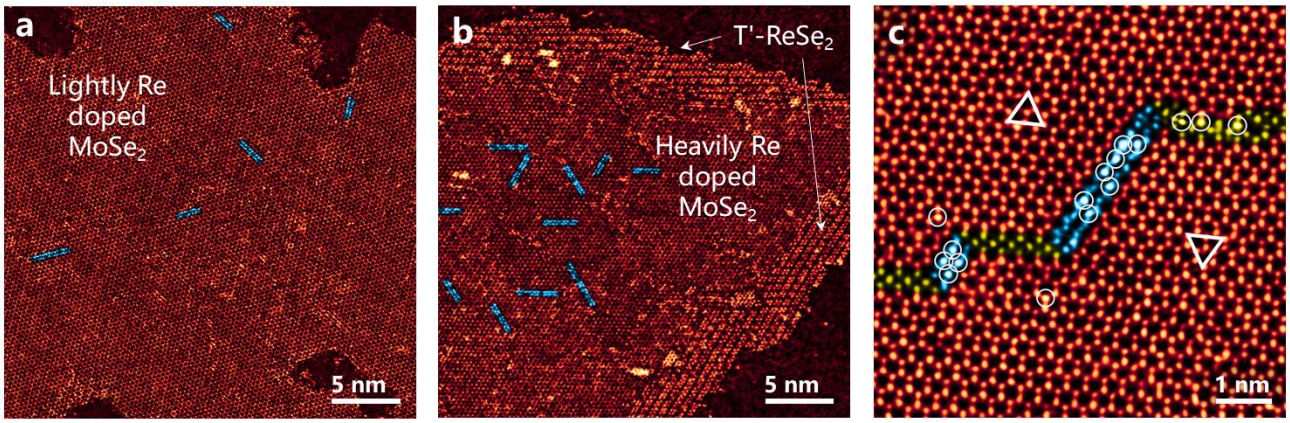

Figure 1. ADF-STEM images depicting the (a) lightly doped $MoSe_2$ and (b) heavily doped $MoSe_2$, respectively. Blue areas in (a) and (b) highlight the presence of MTBs consisting of bright atoms in Re doped $MoSe_2$. T' phase (orthogonal) $ReSe_2$ domains are observed at the edges in (b). (c) Atomically resolved ADF-STEM image from lightly doped samples showing the presence of Re dopants (marked by white circles) occupying the sublattice of Mo within $MoSe_2$ domains and in the MTB regions. The triangles indicate the orientations of the domains.

Ernzernof (PBE) exchange-correlation function. The plane wave cut-off was set to 400 eV. The defects were modelled in a 10×10 supercell, with the Brillouin zone sampled using only the Γ point. Zero eV is set to valence band maximum in electronic structure calculations.

3. Results and discussion

3.1. Distribution of Re dopants and MTBs

Figures 1a and 1b present low magnification ADF-STEM images depicting the morphology of MBE grown lightly and heavily Re doped $MoSe_2$ MLs, respectively. Given that ADF-STEM provides atomic number (Z) contrast[42] and Re is significantly heavier than Mo, we can unambiguously distinguish between the two metal atoms in ADF-STEM images. Notably, in the heavily doped sample (Figure 1b), the ML $MoSe_2$ domain with darker contrast is enclosed by brighter contrast regions resembling rows of adjacent bright lines. These regions, characterized through atomic resolution ADF-STEM, were confirmed to be ML T' phase ML-$ReSe_2$ (detailed in Figure S1 in SI) due to the over Re doping, which is consistent with previous studies[43,44]. Such a H to T' phase transition is attributed to the Peierls distortion induced by the extra d-orbital electron of Re. Excluding T'-$ReSe_2$, bright Re dopants are distributed across the $MoSe_2$ films in both samples with some of them tend to aggregate along MTBs as highlighted by the blue areas in Figures 1a and 1b. The heavily Re doped ML $MoSe_2$ sample exhibits a more pronounced presence of MTBs with the aggregation of bright Re dopants compared to the lightly doped one, implying a correlation between Re doping concentration and the formation of these MTBs.

A representative atomic resolution ADF-STEM image from lightly doped sample is given in Figure 1c showing the location and distribution of Re dopants within a sample area containing an MTB that connects two adjacent $MoSe_2$ domains (located in the upper left and lower right regions with a mirror-symmetry relative to each other). As seen, Re dopants consistently occupy the Mo sublattice sites, i.e. substituting Mo in the doped $MoSe_2$, no matter inside the domains or along the MTB. In this area, the majority of Re dopants (14 out of 16) are predominantly located within the MTB, i.e., an MTB enriched Re dopant, rather than intra-domain. Further statistics will be presented later. Due to the 1D nature of MTB, Re dopants along the MTBs manifest as bright stripes observed in Figures 1a and 1b. In addition to the enrichment of Re observed along the MTBs, we also observe Re enrichment at the edges of the $MoSe_2$ films in the lightly doped sample (detailed in Figure S2 in SI). Thus, the formation of $ReSe_2$ could be hypothetically attributed to the higher chemical reactivity of the $MoSe_2$ edges, wherein a part of Re atoms may be captured by the $MoSe_2$ edges during migration, and subsequently initiating nucleation and growth of $ReSe_2$ locally.

To further uncover the correlation between Re dopants and MTBs, atomic resolution ADF-STEM images and the low-pass filtered[45] ones showing the distribution of Re dopants and MTBs across a large area of undoped, lightly doped, and heavily doped ML $MoSe_2$ samples are presented in Figures 2a-2c and Figures 2d-2f, respectively. The top and bottom panels (a-d, b-e, and c-f) are respectively recorded from the same area where the visibility of Re dopants on the MTBs (marked with white boxes in Figures 2b and 2c) and MTBs (decorated with black boxes in Figures 2e and 2f) is different. As seen, In the undoped sample (Figures 2a and 2d), the MTBs are predominantly aligned along the zigzag direction, forming triangular shaped network with 60° intersection angles, consistent with previously reported findings[40,46]. In contrast, MTBs in the Re doped samples (Figures 2e and 2f) exhibit more intricate geometries than that in undoped sample (Figure 2d), including both 60° angles and additional 120°

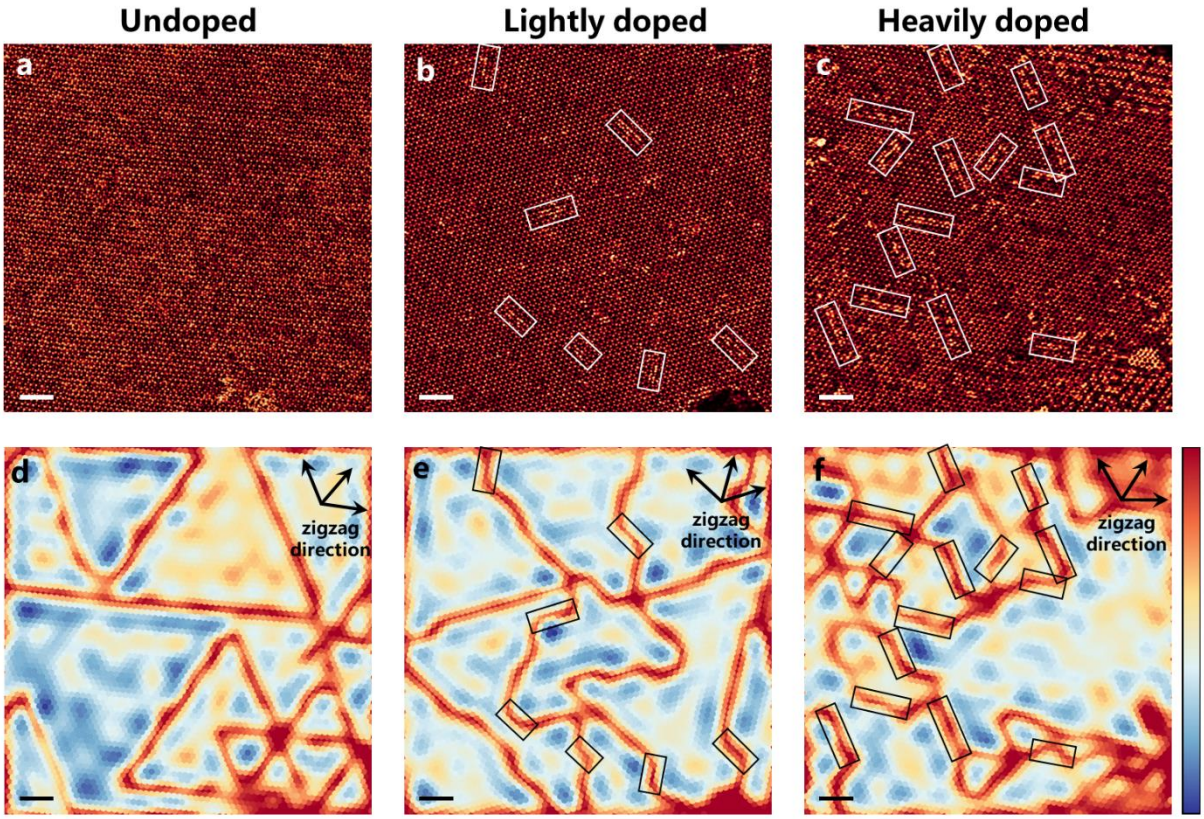

Figure 2. MTB profiles in pristine and Re doped $MoSe_2$ samples. (a-c) ADF-STEM images of (a) undoped $MoSe_2$, (b) lightly Re doped $MoSe_2$, and (c) heavily Re doped $MoSe_2$, respectively. (d-f) Filtered ADF-STEM images corresponding to (a-c) in false colour showing the distribution of MTBs (red lines) in (d) undoped $MoSe_2$, (e) lightly Re doped $MoSe_2$, and (f) heavily Re doped $MoSe_2$, respectively. The blue and red (cold and warm) coloured regions represent hexagonal domains and defective areas like MTBs, respectively. The white boxes in (b) and (c) highlight MTB segments consisting of bright atoms in Re doped $MoSe_2$, and black boxes in (e) and (f) point out the same position which seems to be located at MTBs. Scale bar: 2 nm.

angles (not found in undoped sample) between adjacent MTB segments. Due to the symmetry constrain, for a $MoSe_2$ domain, if one of its edges is X-zz, any of its neighbouring edge with a 60° angle to it must also be X-zz, and those with a 120° angle to it should appear in M-zz configuration. Since the MTBs in undoped $MoSe_2$ are oriented along the X-zz direction, the appearance of 120° angles in the Re doped samples (Figures 2e and 2f) indicates the existence of MTBs along the M-zz direction, which has never been reported in undoped $MoSe_2$ and is energetically unpreferred[47].

3.2. Atomic structure of 4|4E-M MTBs

To elucidate the atomic structure of MTBs along M-zz directions and the distribution of Re atoms within them, we present an atomic resolution ADF-STEM image in Figure 3a. MTBs oriented along X-zz and M-zz directions are highlighted in yellow and blue, respectively. The yellow-highlighted MTBs aligned along the X-zz direction exhibit the typical 4|4P-X configuration. In Figure 3b, a zoom-in image containing a segment of the MTB along M-zz direction is presented, with its atomic structural model overlaid. It is evident that the MTB along M-zz direction behaves as a series of edge-sharing four-member rings, hence named 4|4E-M configuration[47]. This configuration displays a distortion (Figure S3 in SI), akin to the Peierls distortion observed in T'-$ReSe_2$ (the thermodynamically stable phase), which may also arise from the extra electrons introduced by Re dopants[12,48]. Additionally, a discrepancy in coordination emerges between these scenarios, whereas Re atoms exhibit octahedral coordination in T'-$ReSe_2$, they assume trigonal prism coordination in 4|4E-M MTBs.

It is worth noting that there are two reported scenarios[4,24] that can lead to the presence of 120° kinks in 4|4P-X MTBs. The first scenario involves octagonal rings[4], while the second pertains to the 4|4E-M MTBs observed in Nb doped WSe_2[24] and Re doped $MoSe_2$[37]. To explore the potential correlation between these two phenomena, we provide ADF-STEM images (Figures 3c and 3d) for both types of MTB kinks with their atomic structural models superimposed. In Figure 3c, an octagonal ring serves as the kink connecting two segments of 4|4P-X MTBs. Similarly, Figure 3d illustrates a segment of 4|4E-M MTB connecting two 4|4P-X MTB segments. Notably, if we consider the hexagonal ring below the 4|4E-M MTB in Figure 3d as part of

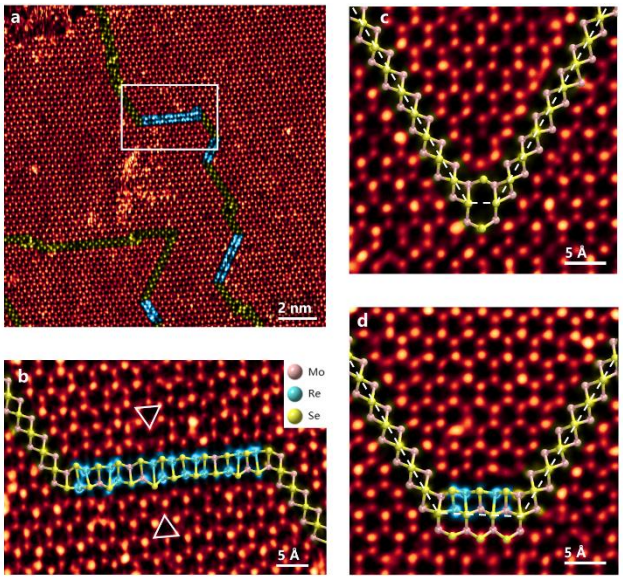

Figure 3. Structure of 4|4E-M MTBs and their relationship with octagonal rings. (a) A representative atomic resolution ADF-STEM image of Re doped $MoSe_2$. 4|4P-X MTBs are highlighted with yellow regions, and 4|4E-M MTBs with blue regions, respectively. (b) Zoom-in image from the white rectangular region in (a) showing the atomic structure of 4|4E-M MTB, where the triangles connecting three metal atoms in one hexagon indicate the orientations of the domains. (c), An ADF-STEM image of an octagonal ring connecting two 4|4P-X MTB segments. (d) An ADF-STEM image of 4|4E-M MTB connecting two 4|4P-X MTB segments.

the MTB structure, it is possible to identify three edge-sharing octagonal rings (with an additional metal atom at the centre of each octagon). Thus, it can be inferred that the 4|4E-M MTB represents a special configuration, an extended form of the octagonal ring, which is induced by Re doping within our samples. Besides, we conducted a statistical analysis to investigate the presence of periodicity in the Re dopants within the MTBs, no discernible periodic pattern was identified.

3.3. Formation of 4|4E-M MTBs induced by Re dopants

We conduct a statistical analysis of the density of Re atoms in various regions and the density of MTBs, with the results presented in Table 1, giving the total Re concentration of approximately 3.0% in atomic percentage (all subsequent concentrations are in atomic percentages) for the lightly doped sample, and 6.8% for the heavily doped sample. In both cases, Re atoms exhibit evident enrichment within MTBs. More than 1/2 and 3/4 of Mo atoms in the 4|4E-M MTB are substituted by Re atoms in the cases of lightly and heavily doped samples, respectively. Furthermore, the Re doping concentration within the $MoSe_2$ domains (non-MTB regions) increases with the increase of overall doping concentration. It is notable that, in terms of percentage increase, the concentration of Re within the $MoSe_2$ domains of the heavily doped sample increases from 1.5% to 2.7% by nearly 1-fold, whereas within the 4|4E-M MTBs, it increases by less than 50% (from 56.4% to 78.1%). This might be attributed to the low Re concentration within the $MoSe_2$ domains, providing ample available Mo sites for substitution, while the concentration of Re within 4|4E-M MTBs is already substantial in the lightly doped sample and thus similar increase cannot be attained. Interestingly, within the 4|4P-X MTBs, both lightly and heavily doped samples present a similar Re doping concentration of approximately 11%. This implies a potential saturation point for Re doping within the 4|4P-X MTBs under our typical MBE conditions. We speculate that this phenomenon might be related to the formation of 4|4E-M MTBs, suggesting that structural transitions might occur in 4|4P-X MTBs once Re doping surpasses a threshold, leading to the formation of 4|4E-M MTBs. This observed threshold concentration of Re in 4|4P-X MTBs may share some similarity with the previously reported thresholds associated with phase transition induced by Re doping[13,29]. The structural changes occur upon exceeding a threshold concentration, which is about 40% for phase transition[13] and about 11% for the formation of 4|4E-M MTBs here. In 4|4P-X MTBs, Re atoms occupy metal sites in a rectangular arrangement. We speculate that as the concentration of Re in MTBs increases, the energy of the rectangular arrangement rises, leading to a structural transformation to 4|4E-M MTBs. The transformed 4|4E-M MTBs may be energetically favourable, since the Re atoms in them adopt a zigzag arrangement at the metal sites, resembling the arrangement found in stable T'-$ReSe_2$ (although with different Se coordination configurations).

The statistical analysis of MTB densities with different configurations provided in Table 1 shows that, as the concentration of Re in the samples increases, the density of 4|4E-M MTBs also increases, providing further evidence for Re dopants' role in the formation of 4|4E-M MTBs.

Table 1. Statistical analyses of Re concentration and the density of MTB

	Concentration of Re dopants (%)				Density of MTB (nm/nm^2)		
	Total*	Pristine domain	4|4P-X	4|4E-M	Total MTB	4|4P-X	4|4E-M
Lightly doped	3.0	1.5	11.3	56.4	0.140	0.119	0.021
Heavily doped	6.8	2.7	10.9	78.1	0.320	0.189	0.131

*Including pristine domain and MTBs.

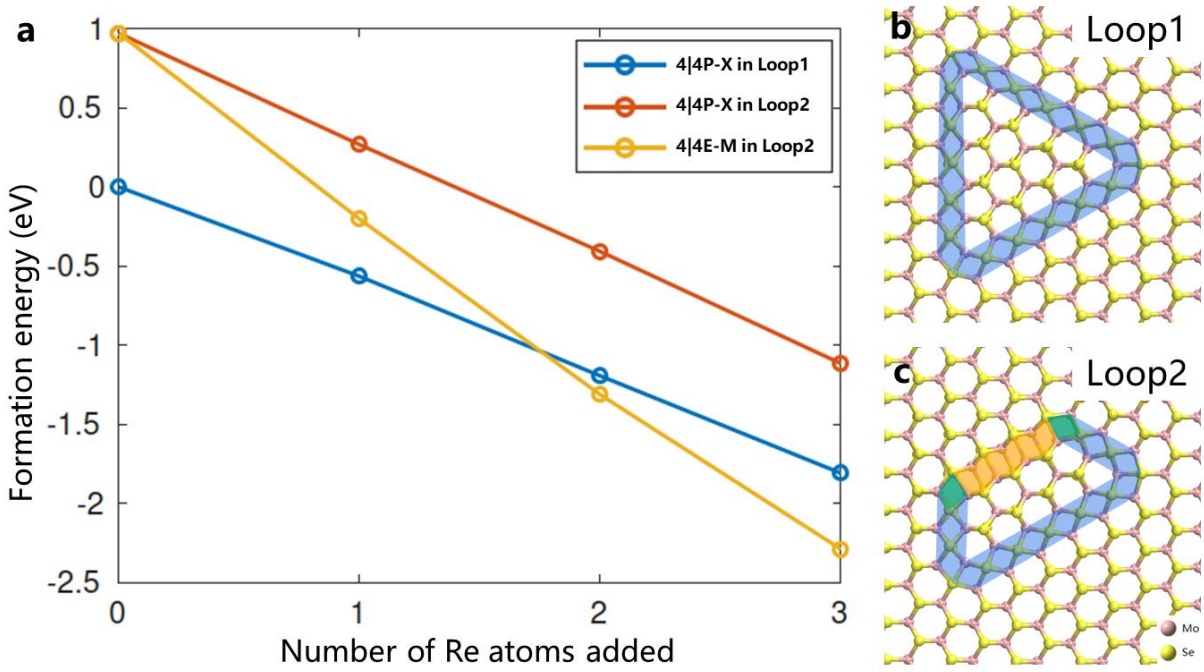

Figure 4. The formation energies of 4|4P-X MTBs and 4|4E-M MTBs with different Re concentration. (a) Formation energy as a function of the number of Re atoms added to (b) MTB Loop1 and (c) MTB Loop2. Loop1 is constructed with three 4|4P-X MTB segments, while Loop2 is constructed with three 4|4P-X MTB segments and one 4|4E-M MTB segment.

Additionally, we observe an increase in the density of 4|4P-X MTBs, which may be attributed to the ability of Re, similar to previously reported transition metals like Mo[35], Nb[24], and V[36], to induce the formation of 4|4P-X MTBs. It is noteworthy that prior to Re deposition, we annealed $MoSe_2$ at 600°C, which reduced the density of 4|4P-X MTBs in $MoSe_2$. This implies that the subsequent introduction of Re simultaneously increases the densities of both types of MTBs, but the overall proportion of 4|4E-M MTBs to total MTBs increases significantly (from 15% in the lightly doped sample to 41% in the heavily doped sample). Combining this observation with the previously discussed threshold of ~11% Re concentration in 4|4P-X MTBs, we speculate that Re atoms, like other transition metals, induce the formation of 4|4P-X MTBs upon their initial incorporation into the $MoSe_2$ films. As the Re concentration within MTBs surpasses the threshold, the 4|4P-X MTBs begin to transform into 4|4E-M MTBs.

DFT calculations are further employed to understand the impact of Re doping on the formation of various MTB configurations, i.e., 4|4P-X and 4|4E-M (Figure 4a), utilizing finite MTB-loop models as depicted in Figures 4b and 4c. In the following, the length of MTBs is defined using the lattice parameter "a" (approximately 3.3 Å) of $MoSe_2$ along the zigzag direction, which corresponds to one four-membered ring for 4|4P-X and two four-membered rings for 4|4E-M, respectively. MTB-loop model I (Loop1 in Figure 4b) is a triangular loop constructed by three 4|4P-X MTB segments, each with a length of 6a. MTB-loop model II (Loop2 in Figure 4c), derived from Loop1 by truncating one corner, has the same number of atoms but consists one 4|4E-M MTB segment with the length of 3a, two shorter 4|4P-X MTB segments with the length of 3a, and one 4|4P-X MTB segment with a length of 6a. Thus, the energy of the MTB-loop model can be written as:

$$\begin{aligned} E(\text{loop}, M, N) = {} & E(\text{pristine}) + n_{\text{Mo}}\mu_{\text{Mo}} \\ & + N\gamma(4|4\text{P}-\text{X}) + M\gamma(4|4\text{E}-\text{M}) \\ & + 2\beta(\text{Se}/\text{Se}) + 2\beta(\text{Se}/\text{Mo}) \end{aligned} \quad (1)$$

where E refers to the total energy, γ is the formation energy per basic unit (edge energy) of the MTB, N (M) is the total length of 4|4P-X (4|4E-M), β is the corner energy, n_{Mo} and μ_{Mo} are the number of added Mo atoms and their chemical potentials, respectively.

Upon increasing the length of a 4|4E-M MTB by 1a, the total length of 4|4P-X MTB decreases by 2a. Then, the total energy of this new loop is:

$$\begin{aligned} E(\text{loop}, M+1, N-2) = {} & E(\text{pristine}) + n_{\text{Mo}}\mu_{\text{Mo}} \\ & + (N-2)\gamma(4|4\text{P}-\text{X}) \\ & + (M+1)\gamma(4|4\text{E}-\text{M}) \\ & + 2\beta(\text{Se}/\text{Se}) + 2\beta(\text{Se}/\text{Mo}) \end{aligned} \quad (2)$$

Comparing Equations (1) and (2), the edge energy for 4|4E-M MTB can be derived as:

$$\begin{aligned} \gamma(4|4\text{E}-\text{M}) = {} & E(\text{loop}, M+1, N-2) \\ & - E(\text{loop}, M, N) + 2\gamma(4|4\text{P}-\text{X}) \end{aligned} \quad (3)$$

The calculated energy difference between E(loop,3,12) and E(loop,2,14) is 0.245 eV according to DFT, and γ(4|4P-X) is taken as 0.1 eV (at Mo-rich limit) from literature[30,47], we could obtain γ(4|4E-M) as approximately 0.45 eV. Since the edge energy of 4|4E-M (0.45 eV) is higher than that of 4|4P-X (0.1 eV), one would not expect to see a high density of 4|4E-M MTBs.

The above analysis is based on pristine $MoSe_2$ system with no extrinsic dopants. To approach the experimental results, we now proceed to substitute some of the Mo atoms in MTBs with Re dopants for both the 4|4P-X in Loop1, 4|4P-X and 4|4E-M in Loop2. The formation energies of these systems are calculated with the number of Re dopants up to 3. The formation energy is defined as:

$$E_{\mathrm{f}} = E(\mathrm{loop} + \mathrm{Re}) - E(\mathrm{loop}, 0{,}18) + n_{\mathrm{Re}}[E(\mathrm{Re_{Mo}}) - E(\mathrm{pristine})] \quad (4)$$

Here, the formation energy is given in relative to the Loop1 without Re dopants, and [E(Re_{Mo})-E(pristine)] stands for the formation energy of a single Re_{Mo} substitutional defect in a perfect $MoSe_2$ lattice.

Formation energies of three systems are calculated with the number of Re dopants varying from 0 to 3 are calculated and plotted in Figure 4a. In the absence of Re dopant, Loop2 (yellow and red) has higher formation energies compared to Loop1 (blue). After the Re substitution, the formation energy decreases across all three cases where the reduction for the case of 4|4E-M MTB is more profound. As read from Figure 4a, after the incorporation of two Re dopants into the subject MTB (corresponding to a 33.3% of Re_{Mo} defects), Loop2 becomes energetically favourable, over Loop1, indicating the Re_{Mo} defect (substituting Mo with Re) can stabilize the MTB-loop system for both 4|4P-X and 4|4E-M. In specific, such stabilization effect is more pronounced for the 4|4E-M case

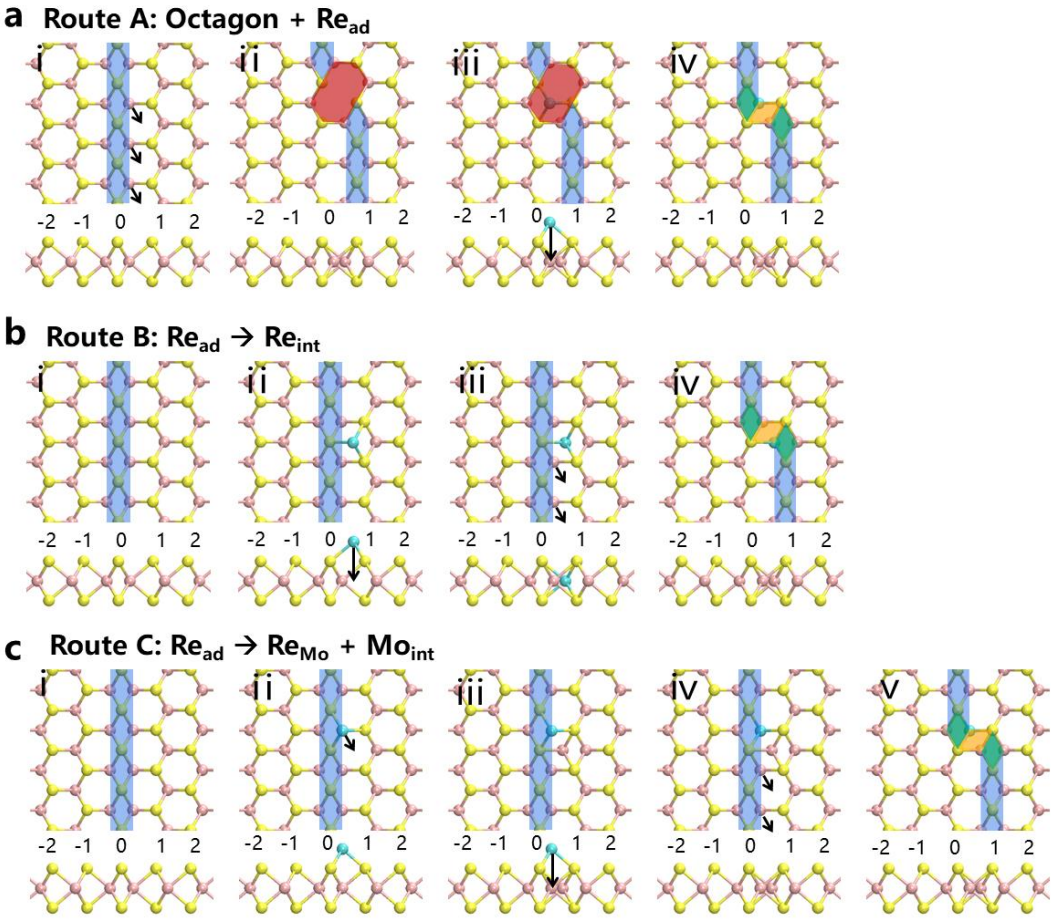

Figure 5. Three possible formation routes of Re doped 4|4E-M MTBs. (a) Route A: first, the Mo atoms arrowed on the 4|4P-X MTB are displaced to the centre of the hexagonal rings, leading to the formation of an octagonal ring (red), after which Re_{ad} incorporates into the octagonal ring to form a 4|4E-M MTB segment. (b) Route B: a Re_{ad} incorporates into the domain as a Re_{int} next to a 4|4P-X MTB (in blue), and then the 4|4E-M MTB segment forms after displacement of Mo atoms. (c) Route C: a Re_{ad} replaces the Mo atom on the 4|4P-X MTB, resulting a Mo_{int} and a Re_{Mo} in the MTB, thus a 4|4E-M MTB segment forms via displacement of Mo atoms. The top and side views of the incorporation process are illustrated in each panel. The red, blue, yellow, and green areas indicate the octagonal rings, 4|4P-X MTBs, 4|4E-M MTBs, the four-member rings shared by 4|4P-X and 4|4E-M MTBs, respectively.

than the 4|4P-X. Such a trend is consistent when the Re doping concentration further increases. This result indicates that 4|4E-M MTBs observed in our experiments can be attributed to the high concentration of Re doping into MTBs (Recall that the Re doping ratio reaches 56.4% or even 78.1% within the MTB as shown in Table 1).

Above experimental analysis and DFT calculation enable us to propose several formation routes for the 4|4P-X MTBs in Re doped $MoSe_2$ as shown Figures 5a-5c. All routes start from a single straight 4|4P-X MTB and involve two main steps, Mo displacement and Re insertion, although differing in the order of these processes and the atomic details of the Re insertion. Start from Route A (Figure 5a), it involves first displacement of Mo atoms from their regular sites within the MTB to the centres of neighbouring hexagons, resulting in the formation of an octagonal ring and the right moving of the bottom MTB segment by one unit (ii in Figure 5a). Subsequently, when Re atoms are introduced as adatoms (Re_{ad}), seeking energetically favourable adsorption sites, such as the octagonal rings that provide more space than other sites (iii in Figure 5a). Once Re_{ad} is incorporated into the octagonal ring, the 4|4E-M MTB is formed (iv in Figure 5a).

In routes B and C, the Re is inserted into the lattice before Mo displacement. If there is no octagonal ring, it is reasonable to assume the Re_{ad} prefers to stay along the MTBs due to the strain effect, and its exact site can be either above the centre of hexagon (ii in Figure 5b) or above a Mo atom (ii in Figure 5c). More specifically, in route B, the Re_{ad} then incorporates into the lattice (iii in Figure 5b), becoming an interstitial defect (Re_{int}). Differently in route C, the Re_{ad} occupies the sublattice of the Mo atom beneath after the original Mo atom shifts to the centre of hexagon (iii in Figure 5c), resulting in a Mo

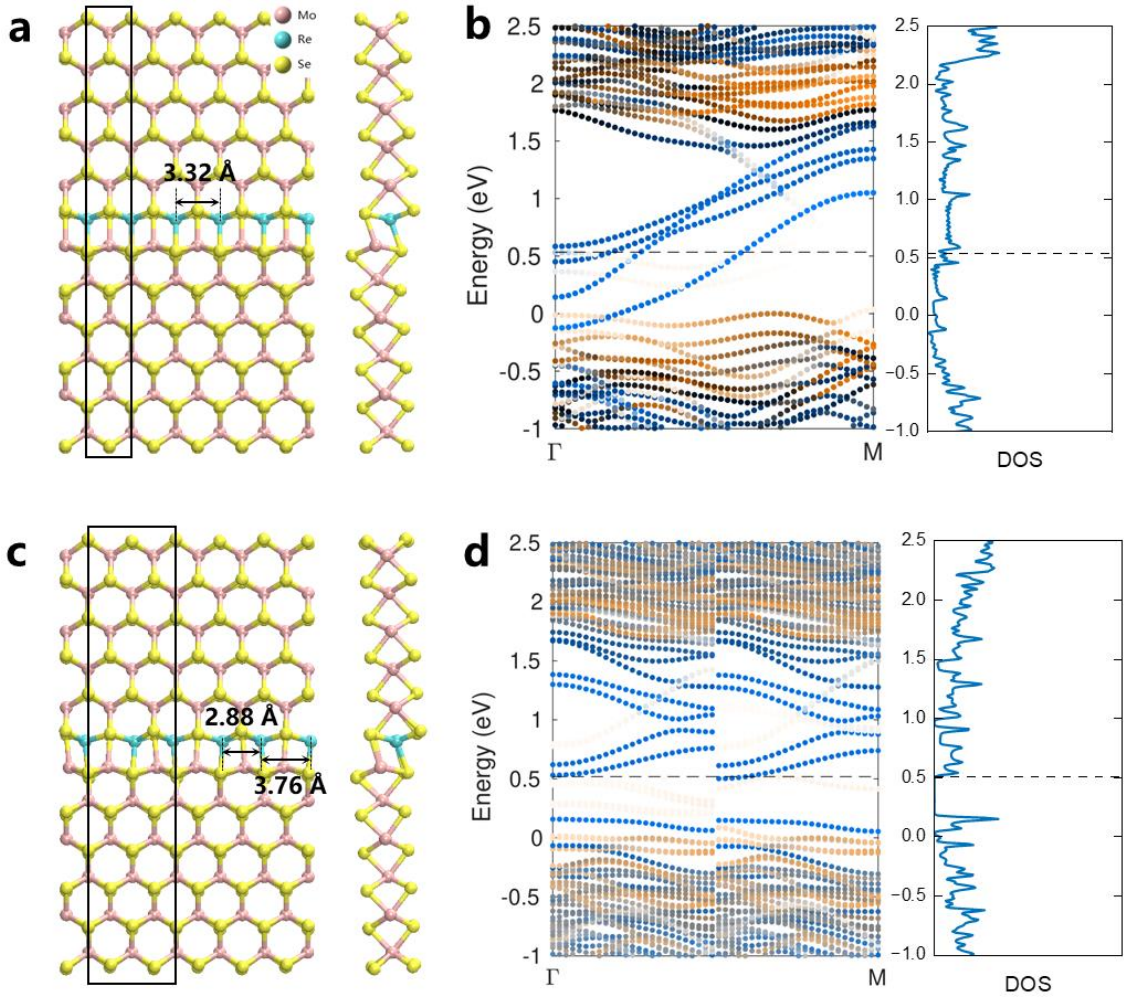

Figure 6. DFT calculated band structures and DOSs of 4|4E-M MTBs. (a, c) The top and side view of (a) unit cell and (c) super cell models with a 50% Re substitution to the Mo atoms in 4|4E-M MTBs. The cells used in calculations are indicated by black rectangles. The super cell structure model in (c) shows a distortion. (b, d) The band structures (left panels) and DOSs localized in 4|4E-M MTBs (right panels) calculated by (b) unit cell and (d) super cell models. Spin-up and spin-down band structures are shown in (d). Blue lines: pristine $MoSe_2$ bands, orange lines: 4|4E-M MTB bands.

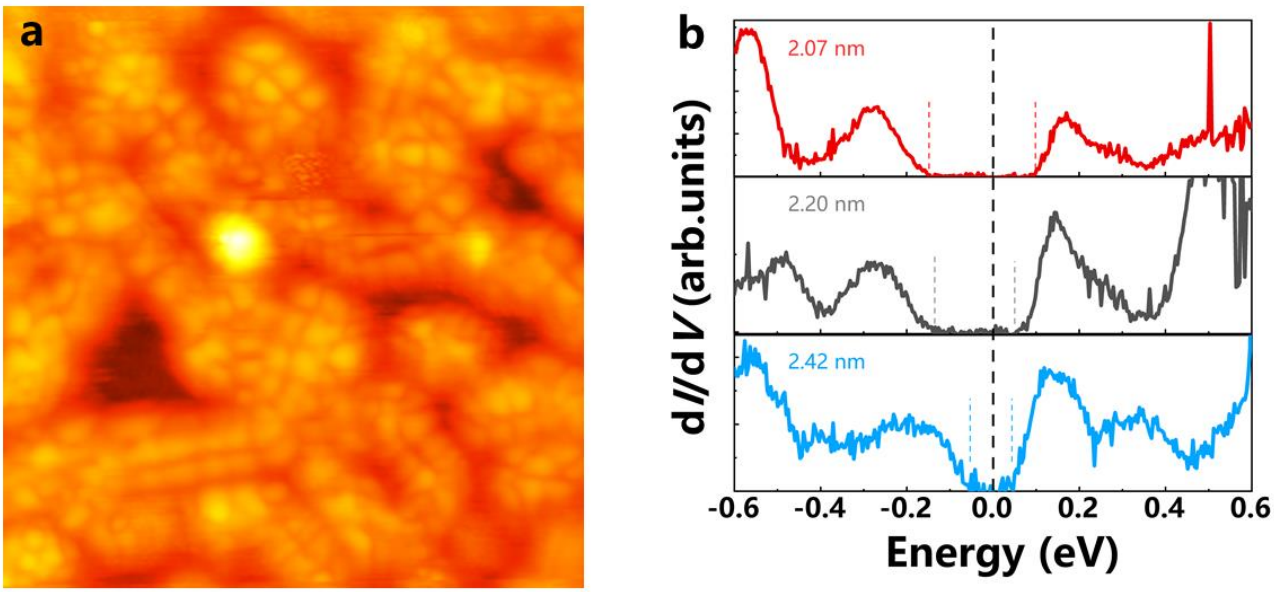

Figure 7. Experimental results from STM/S. The typical STM images of (a) Re doped ML $MoSe_2$ (20 nm × 20 nm. Bias -0.2 V). (b) STS spectra captured from three MTBs with different length in Re doped ML $MoSe_2$ sample.

interstitial (Mo_{int}) and a substitutional defect (Re_{Mo}). After the formation of Re_{int} in Route B and Re_{Mo} and Mo_{int} in Route C, the atomic configurations in two systems are essentially the same, except for the exchanged positions of Re and Mo atom. Both are then followed by the Mo displacement to yield 4|4E-M MTB (iv in Figures 5b and 5c). Repeating these processes, more Re atoms are incorporated into the $MoSe_2$, and the product 4|4E-M MTBs progressively extend.

3.4. Electronic structure of 4|4E-M MTBs

We then calculate electronic structures of 4|4E-M MTBs. We first calculate using the unit cell model, as illustrated in Figure 6a. And Figure 6b present the resulting band structure and density of states (DOS). In Figure 6a, the structural model depicts a 50% concentration of Re within the MTB, comparable to our statistical findings (56.4%) in the lightly doped sample. Both the band structure and DOS (Figure 6b) reveal the presence of electron-like bands localized at the MTBs, crossing the Fermi level (the dashed horizontal line), indicating a metallic behavior of MTBs. Notably, there are four MTB bands in the gap, likely originating from the broken symmetry in the out-of-plane direction shown in the side view (Figure 6a). In addition to the 50% concentration, we have also calculated scenarios with 0% and 100% Re concentration (Figures S4a-d in ESI†). As the Re concentration increases, the bands shift to lower energy while the Fermi-level remains at the same level. In other words, the MTB bands are occupied at higher levels due to the extra electrons from Re dopants. For comparison we also calculated the band structures of 4|4P-X MTBs (Figure S5 in ESI†). They also exhibit a similar trend, i.e., the bands shift to lower energies with increasing Re concentration. Electronic conductivity of 4|4E-M MTB should be superior to that of 4|4P-X MTB as it contains more metallic bands crossing Fermi level (four vs. two).

We further perform DFT calculations on the electronic structures of 4|4E-M MTBs at 0%, 50%, and 100% Re concentrations using a super cell (twice the size of the unit cell) model. Figures 6c and 6d display the structural models utilized for DFT calculations and the resulting band structure and DOS at 50% Re concentration, while the remaining scenarios are presented in Figures S4e-h in ESI†. Notably, periodic atomic distortions within 4|4E-M MTBs are observed in Figure 6c, absent in the undistorted structure of Figure 6a. This periodic distortion is more pronounced within the metal sublattice, evidenced by the lateral distances between adjacent metal atoms in Figure 6a (3.32 Å) transitioning to periodic variations of adjacent Re atoms at 2.88 Å and 3.76 Å, as well as adjacent Mo atoms at 2.92 Å and 3.72 Å in Figure 6c. This periodic distortion aligns with the distortion observed in our ADF-STEM results (Figure S3a in ESI†). In comparison to the undistorted structure of Figure 6a, this distortion leads to a reduction of system energy and opens a gap of ~0.3 eV. Through a comparative analysis of DFT calculations for three distinct Re concentrations within the MTB, we note an increase in the degree of distortion with rising Re concentration. Assessing the difference in periodic Re/Mo atomic distances as a metric, we observe values of 52 pm at 0%, 80 pm for Mo and 88 pm for Re at 50%, and 90 pm at 100% Re concentrations, respectively. Moreover, the gap size diminishes with increasing Re concentration, decreasing from ~0.5 eV at 0% to ~0.3 eV at 50%. At 100% Re concentration within 4|4E-M MTB, two electron-like bands intersect the Fermi level, indicating a metallic behavior.

Low-temperature STM/S is utilized to experimentally reveal the electronic structure of 4|4E-M MTBs (Figure 7). As

seen from STM, the morphology of MTBs in Re doped $MoSe_2$ (Figure 7a) are quite different from conventional 4|4P-X MTBs in as-grown (non-doped) $MoSe_2$ samples[34]: MTBs in Re doped $MoSe_2$ distribute randomly without a uniform wagon-wheel arrangement as the 4|4P-X MTBs do. However, similar to 4|4P-X MTBs, STM reveals the presence of a 3*a* periodicity (~1 nm) charge modulation at the MTB sites. Additionally, STS measurements unveil the existence of small energy gaps in the electronic structure of 4|4E-M MTBs. Further STS measurements on various MTBs find the gap sizes have a relatively large variation depending on the MTB lengths, typical examples are shown in Figure 7b. With increasing MTB length, the gap size diminishes from 0.24 eV to 0.10 eV. Given the presence of gaps in all STS measurements, it is evident that the existence of this gap cannot be solely attributed to quantum confinement effects.

Both CDW and quantum confined TLL could account for the observed gap openings in the 4|4E-M MTBs. In our ADF-STEM experiments, we observe a distortion in 4|4E-M MTBs (akin to the Peierls distortion observed in T'-$ReSe_2$), which is also found in DFT calculations, both supporting the presence of CDW. However, the experimentally observed distortion is not as periodic as indicated by the DFT calculations. This discrepancy may stem from the fact that the actual behavior of Re atoms substituting Mo atoms deviates from the periodicity assumed in the computational models. Additionally, while both ADF-STEM and DFT results reveal a distortion with a periodicity of twice the lattice constant (2*a*), the charge modulation observed in low-temperature STM corresponds to a 3*a* periodicity. This misalignment between the periodicities of lattice distortion and charge modulation suggests that the lattice distortion we observe may not be the primary cause of the observed gap.

Next, we turn our attention to the variation in gap sizes observed in the STS experiments. Previous reports suggested that Peierls-type CDW gap sizes would remain consistent across different intrinsic MTBs[31,32,49]. In terms of MTBs induced by extrinsic doping such as Re atoms, the varying Re concentrations in MTBs here may influence the CDW gap size. The DFT results suggest that with increasing Re concentration in 4|4E-M MTBs, the gap size diminishes, until all Mo atoms in the MTB are replaced by Re, resulting in metallic behaviour. Therefore, CDW with different Re concentrations could account for the observed variation of gap sizes. Besides CDW, quantum confined TLL could also lead to observed gap variations, as the electron-electron interaction induced gap sizes depend on the MTB length ($E_g \sim 1/L$)[33,34]. Indeed, typical STS spectra in Figure 7b show different gap sizes with respect to different MTB lengths. While STS experimental results indicate a trend of decreasing gap size with increasing MTB length, the small variation in MTB lengths in our samples (ranging from 2 to 5 nm) precludes a definitive statistical analysis.

The rigorous proving of the TLL nature of the MTBs in Re doped $MoSe_2$ would require more experimental verifications, such as STS measured from the same MTB but at various temperatures, and fittings of STS spectra taken on long MTBs to the theoretical predicted power-law suppression at the Fermi level. Based on present results, we can only confidently conclude the following: i. There is a consistent presence of gaps at the Fermi level; ii. The gap sizes vary among MTBs, indicative of quantum confined TLL or Peierls-type CDW under different Re concentration.

Indeed, if the MTBs in Re doped $MoSe_2$ are confirmed to be TLLs, the electron-electron interaction could be stronger than that in 4|4P-X MTBs in $MoSe_2$ as Re atoms provide extra electrons confined in the 1D metallic system (verifications are needed both theoretically and experimentally as their atomic structure are not the same). As a result, this could lead to an elevated charge velocity. If the spin-rotation invariance is retained, one could expect a larger separation between charge and spin velocities, which is favourable in physics research.

4. Conclusion

We have successfully fabricated ML $MoSe_2$ samples with varying levels of Re doping using MBE. Utilizing atomic resolution ADF-STEM, we have identified a novel MTB configuration termed 4|4E-M. By means of statistical analysis of Re concentration and MTB density, in conjunction with DFT calculations, we attributed the primary cause of 4|4E-M MTB formation to Re doping and proposed possible routes for the formation of 4|4E-M MTBs: Re atoms tend to substitute for Mo atoms within MTBs, and as Re doping concentration increases, the 4|4E-M configuration becomes energetically more stable compared to the 4|4P-X configuration, thus prompting the emergence of 4|4E-M MTBs. The electronic structures of MTBs in Re doped $MoSe_2$ were also studied via DFT and STM/S, potentially attributed to CDW or quantum confined TLL. Our work not only expands our understanding of defect engineering in 2D TMDs but also opens new avenues for exploring novel physical phenomena.

Author Contributions

Zhoubin Yu: Conceptualization, Data curation, Formal analysis, Investigation, Writing - Original Draft

Yipu Xia: Conceptualization, Resources, Formal analysis, Investigation, Writing - Original Draft

Hannu-Pekka Komsa: Methodology, Formal analysis, Writing - Review & Editing

Junqiu Zhang: Formal analysis, Investigation

Maohai Xie: Funding acquisition, Writing - Review & Editing

Chuanhong Jin: Funding acquisition, Writing - Review & Editing

Conflicts of interest

There are no conflicts to declare.

Acknowledgements

This work was financially supported by the National Natural Science Foundation of China under Grant Nos. 51761165024 and 61721005, the National Key R&D Program of China under the grant No. 2022YFB4401602, the Zhejiang Provincial Natural Science Foundation under Grant No. LD19E020002. This work was also supported by the Basic and Applied Basic Research Major Programme of Guangdong Province, China (Grant No. 2021B0301030003) and Jihua Laboratory (Project No. X210141TL210). MHX acknowledges the support from the Research Grant Council of Hong Kong Special Administrative Region, China (Nos. N_HKU732/17, C7036-17W, and AoE/P-701/20). We also wish to acknowledge the Center of Electron Microscopy of Zhejiang University and CSC-IT Center for Science, Finland for the access to microscope facilities and computational resources, respectively.

References

[1] Radisavljevic B, Radenovic A, Brivio J, Giacometti V and Kis A 2011 Single-layer MoS_2 transistors *Nat. Nanotechnol.* **6** 147–50

[2] Yin Z, Li H, Li H, Jiang L, Shi Y, Sun Y, Lu G, Zhang Q, Chen X and Zhang H 2012 Single-Layer MoS_2 Phototransistors *ACS Nano* **6** 74–80

[3] Lukowski M A, Daniel A S, Meng F, Forticaux A, Li L and Jin S 2013 Enhanced Hydrogen Evolution Catalysis from Chemically Exfoliated Metallic MoS_2 Nanosheets *J. Am. Chem. Soc.* **135** 10274–7

[4] Zhou W, Zou X, Najmaei S, Liu Z, Shi Y, Kong J, Lou J, Ajayan P M, Yakobson B I and Idrobo J-C 2013 Intrinsic Structural Defects in Monolayer Molybdenum Disulfide *Nano Lett.* **13** 2615–22

[5] Li L and Carter E A 2019 Defect-Mediated Charge-Carrier Trapping and Nonradiative Recombination in WSe_2 Monolayers *J. Am. Chem. Soc.* **141** 10451–61

[6] Zhao X, Ji Y, Chen J, Fu W, Dan J, Liu Y, Pennycook S J, Zhou W and Loh K P 2019 Healing of Planar Defects in 2D Materials via Grain Boundary Sliding *Adv. Mater.* **31** 1900237

[7] Xia Y, Ding D, Xiao K, Zhang J, Xu S, He D, Yue X, Rao Q, Wang X, Ding S, Gao G, Xue H, Wang Y, Yuan M, Ho W, Ki D, Xu H, Cui X, Jin C and Xie M 2023 Wafer-scale single-crystalline $MoSe_2$ and WSe_2 monolayers grown by molecular-beam epitaxy at low-temperature — the role of island-substrate interaction and surface steps *Nat. Sci.* **3** 20220059

[8] Zheng Y J, Chen Y, Huang Y L, Gogoi P K, Li M-Y, Li L-J, Trevisanutto P E, Wang Q, Pennycook S J, Wee A T S and Quek S Y 2019 Point Defects and Localized Excitons in 2D WSe_2 *ACS Nano* **13** 6050–9

[9] Zhang X, Wang S, Lee C-K, Cheng C-M, Lan J, Li X, Qiao J and Tao X 2020 Unravelling the effect of sulfur vacancies on the electronic structure of the MoS_2 crystal *Phys. Chem. Chem. Phys.* **22** 21776–83

[10] Batzill M 2018 Mirror twin grain boundaries in molybdenum dichalcogenides *J. Phys. Condens. Matter* **30** 493001

[11] Cheng J, Jiang T, Ji Q, Zhang Y, Li Z, Shan Y, Zhang Y, Gong X, Liu W and Wu S 2015 Kinetic Nature of Grain Boundary Formation in As-Grown MoS_2 Monolayers *Adv. Mater.* **27** 4069–74

[12] Kochat V, Apte A, Hachtel J A, Kumazoe H, Krishnamoorthy A, Susarla S, Idrobo J C, Shimojo F, Vashishta P, Kalia R, Nakano A, Tiwary C S and Ajayan P M 2017 Re Doping in 2D Transition Metal Dichalcogenides as a New Route to Tailor Structural Phases and Induced Magnetism *Adv. Mater.* **29** 1703754

[13] Shi W, Wang Z and Fu Y Q 2017 Rhenium doping induced structural transformation in mono-layered MoS_2 with improved catalytic activity for hydrogen evolution reaction *J. Phys. D. Appl. Phys.* **50** 405303

[14] Qiu H, Xu T, Wang Z, Ren W, Nan H, Ni Z, Chen Q, Yuan S, Miao F, Song F, Long G, Shi Y, Sun L, Wang J and Wang X 2013 Hopping transport through defect-induced localized states in molybdenum disulphide *Nat. Commun.* **4** 2642

[15] Hu J, Yu L, Deng J, Wang Y, Cheng K, Ma C, Zhang Q, Wen W, Yu S, Pan Y, Yang J, Ma H, Qi F, Wang Y, Zheng Y, Chen M, Huang R, Zhang S, Zhao Z, Mao J, Meng X, Ji Q, Hou G, Han X, Bao X, Wang Y and Deng D 2021 Sulfur vacancy-rich MoS_2 as a catalyst for the hydrogenation of CO_2 to methanol *Nat. Catal.* **4** 242–50

[16] Gao H, Suh J, Cao M C, Joe A Y, Mujid F, Lee K-H, Xie S, Poddar P, Lee J-U, Kang K, Kim P, Muller D A and Park J 2020 Tuning Electrical Conductance of MoS_2 Monolayers through Substitutional Doping *Nano Lett.* **20** 4095–101

[17] Wang S, Cavin J, Hemmat Z, Kumar K, Ruckel A, Majidi L, Gholivand H, Dawood R, Cabana J, Guisinger N, Klie R F, Khalili-Araghi F, Mishra R and Salehi-Khojin A 2020 Phase-Dependent Band Gap Engineering in Alloys of Metal-Semiconductor Transition Metal Dichalcogenides *Adv. Funct. Mater.* **30** 2004912

[18] Xia Y, Zhang J, Yu Z, Jin Y, Tian H, Feng Y, Li B, Ho W, Liu C, Xu H, Jin C and Xie M 2020 A Shallow Acceptor of Phosphorous Doped in $MoSe_2$ Monolayer *Adv. Electron. Mater.* **6** 1900830

[19] Kim K H, Kim K S, Ji Y J, Moon I, Heo K, Kang D-H, Kim K N, Yoo W J, Park J-H and Yeom G Y 2020 Effect of large work function modulation of MoS_2 by controllable chlorine doping using a remote plasma *J. Mater. Chem. C* **8** 1846–51

[20] Gong Y, Liu Z, Lupini A R, Shi G, Lin J, Najmaei S, Lin Z, Elías A L, Berkdemir A, You G, Terrones H, Terrones M, Vajtai R, Pantelides S T, Pennycook S J, Lou J, Zhou W and Ajayan P M 2014 Band Gap Engineering and Layer-by-Layer Mapping of Selenium-Doped Molybdenum Disulfide *Nano Lett.* **14** 442–9

[21] Lin Y-R, Cheng W-H, Richter M H, DuChene J S, Peterson E A, Went C M, Al Balushi Z Y, Jariwala D, Neaton J B, Chen L-C and Atwater H A 2020 Band Edge Tailoring in Few-Layer Two-Dimensional Molybdenum Sulfide/Selenide Alloys *J. Phys. Chem. C* **124** 22893–902

[22] Zhang J, Zhu Y, Tebyetekerwa M, Li D, Liu D, Lei W, Wang L, Zhang Y and Lu Y 2021 Vanadium-Doped Monolayer MoS_2 with Tunable Optical Properties for Field-Effect Transistors *ACS Appl. Nano Mater.* **4** 769–77

[23] Qin Z, Loh L, Wang J, Xu X, Zhang Q, Haas B, Alvarez C, Okuno H, Yong J Z, Schultz T, Koch N, Dan J, Pennycook S J, Zeng D, Bosman M and Eda G 2019 Growth of Nb-Doped Monolayer WS_2 by Liquid-Phase Precursor Mixing *ACS Nano* **13** 10768–75

[24] Wang B, Xia Y, Zhang J, Komsa H-P, Xie M, Peng Y and Jin C 2020 Niobium doping induced mirror twin boundaries in MBE grown WSe_2 monolayers *Nano Res.* **13** 1889–96

[25] Loh L, Chen Y, Wang J, Yin X, Tang C S, Zhang Q, Watanabe K, Taniguchi T, Wee A T, Bosman M, Quek S Y and Eda G 2021 Impurity-Induced Emission in Re-Doped WS_2 Monolayers *Nano Lett.* **21** 5293–300

[26] Li S, Hong J, Gao B, Lin Y, Lim H E, Lu X, Wu J, Liu S, Tateyama Y, Sakuma Y, Tsukagoshi K, Suenaga K and Taniguchi T 2021 Tunable Doping of Rhenium and Vanadium into Transition Metal Dichalcogenides for Two-Dimensional Electronics *Adv. Sci.* **8** 202004438

[27] Zhang K, Feng S, Wang J, Azcatl A, Lu N, Addou R, Wang N, Zhou C, Lerach J, Bojan V, Kim M J, Chen L-Q, Wallace R M, Terrones M, Zhu J and Robinson J A 2015 Manganese Doping of Monolayer MoS_2 : The Substrate Is Critical *Nano Lett.* **15** 6586–91

[28] Sharona H, Vishal B, Bhat U, Paul A, Mukherjee A, Sarma S C, Peter S C and Datta R 2019 Rich diversity of crystallographic phase formation in 2D $Re_xMo_{1-x}S_2$ (x<0.5) alloy *J. Appl. Phys.* **126** 224302

[29] Yang S-Z, Gong Y, Manchanda P, Zhang Y-Y, Ye G, Chen S, Song L, Pantelides S T, Ajayan P M, Chisholm M F and Zhou W 2018 Rhenium-Doped and Stabilized MoS_2 Atomic Layers with Basal-Plane Catalytic Activity *Adv. Mater.* **30** 1803477

[30] Komsa H-P and Krasheninnikov A V. 2017 Engineering the Electronic Properties of Two-Dimensional Transition Metal Dichalcogenides by Introducing Mirror Twin Boundaries *Adv. Electron. Mater.* **3** 1600468

[31] Barja S, Wickenburg S, Liu Z-F, Zhang Y, Ryu H, Ugeda M M, Hussain Z, Shen Z-X, Mo S-K, Wong E, Salmeron M B, Wang F, Crommie M F, Ogletree D F, Neaton J B and Weber-Bargioni A 2016 Charge density wave order in 1D mirror twin boundaries of single-layer $MoSe_2$ *Nat. Phys.* **12** 751–6

[32] Wang L, Wu Y, Yu Y, Chen A, Li H, Ren W, Lu S, Ding S, Yang H, Xue Q, Li F and Wang G 2020 Direct Observation of One-Dimensional Peierls-type Charge Density Wave in Twin Boundaries of Monolayer $MoTe_2$ *ACS Nano* **14** 8299–306

[33] Jolie W, Murray C, Weiß P S, Hall J, Portner F, Atodiresei N, Krasheninnikov A V, Busse C, Komsa H, Rosch A and Michely T 2019 Tomonaga-Luttinger Liquid in a Box: Electrons Confined within MoS_2 Mirror-Twin Boundaries *Phys. Rev. X* **9** 011055

[34] Xia Y, Zhang J, Jin Y, Ho W, Xu H and Xie M 2020 Charge Density Modulation and the Luttinger Liquid State in $MoSe_2$ Mirror Twin Boundaries *ACS Nano* **14** 10716–22

[35] Coelho P M, Komsa H-P, Coy Diaz H, Ma Y, Krasheninnikov A V. and Batzill M 2018 Post-Synthesis Modifications of Two-Dimensional $MoSe_2$ or $MoTe_2$ by Incorporation of Excess Metal Atoms into the Crystal Structure *ACS Nano* **12** 3975–84

[36] Pathirage V, Lasek K, Krasheninnikov A V, Komsa H P and Batzill M 2023 Mirror twin boundaries in WSe_2 induced by vanadium doping *Mater. Today Nano* **22** 100314

[37] Zhang J, Xia Y, Yu Z, Yue X, Jin Y, Yuan M, Feng Y, Li B, Wang B, Ho W, Liu C, Xu H, Jin C and Xie M 2023 Niobium and rhenium doping in $MoSe_2$ monolayer during molecular beam epitaxy: Shallow dopants and defect proliferation *APL Mater.* **11** 071113

[38] Lin Y-C, Björkman T, Komsa H-P, Teng P-Y, Yeh C-H, Huang F-S, Lin K-H, Jadczak J, Huang Y-S, Chiu P-W, Krasheninnikov A V. and Suenaga K 2015 Three-fold rotational defects in two-dimensional transition metal dichalcogenides *Nat. Commun.* **6** 6736

[39] Liu H, Jiao L, Yang F, Cai Y, Wu X, Ho W, Gao C, Jia J, Wang N, Fan H, Yao W and Xie M 2014 Dense Network of One-Dimensional Midgap Metallic Modes in Monolayer $MoSe_2$ and Their Spatial Undulations *Phys. Rev. Lett.* **113** 066105

[40] Hong J, Wang C, Liu H, Ren X, Chen J, Wang G, Jia J, Xie M, Jin C, Ji W, Yuan J and Zhang Z 2017 Inversion Domain Boundary Induced Stacking and Bandstructure Diversity in Bilayer $MoSe_2$ *Nano Lett.* **17** 6653–60

[41] Xia Y, Wang B, Zhang J, Jin Y, Tian H, Ho W, Xu H, Jin C and Xie M 2020 Quantum Confined Tomonaga-Luttinger Liquid in Mo_6Se_6 Nanowires Converted from an Epitaxial $MoSe_2$ Monolayer *Nano Lett.* **20** 2094–9

[42] Krivanek O L, Chisholm M F, Nicolosi V, Pennycook T J, Corbin G J, Dellby N, Murfitt M F, Own C S, Szilagyi Z S, Oxley M P, Pantelides S T and Pennycook S J 2010 Atom-by-atom structural and chemical analysis by annular dark-field electron microscopy *Nature* **464** 571–4

[43] Chen B, Li H, Liu H, Wang X, Xie F, Deng Y, Hu W, Davey K, Zhao N and Qiao S 2019 1T′-ReS_2 Confined in 2D-Honeycombed Carbon Nanosheets as New Anode Materials for High-Performance Sodium-Ion Batteries *Adv. Energy Mater.* **9** 1901146

[44] Fei Z, Wang B, Ho C-H, Lin F, Yuan J, Zhang Z and Jin C 2017 Direct identification of monolayer rhenium diselenide by an individual diffraction pattern *Nano Res.* **10** 2535–44

[45] Yu Z, Dai Y, Komsa H-P, Ren X, Yuan M, Xie M and Jin C 2023 Formation mechanism of mirror twin grain boundaries in molecular beam epitaxy grown monolayer WSe_2-$MoSe_2$ lateral heterojunctions *2D Mater.* **10** 035010

[46] Lin J, Pantelides S T and Zhou W 2015 Vacancy-Induced Formation and Growth of Inversion Domains in Transition-Metal Dichalcogenide Monolayer *ACS Nano* **9** 5189–97

[47] Lehtinen O, Komsa H-P, Pulkin A, Whitwick M B, Chen M-W, Lehnert T, Mohn M J, Yazyev O V., Kis A, Kaiser U and Krasheninnikov A V. 2015 Atomic Scale Microstructure and Properties of Se-Deficient Two-Dimensional $MoSe_2$ *ACS Nano* **9** 3274–83

[48] Lin Y-C, Komsa H-P, Yeh C-H, Björkman T, Liang Z-Y, Ho C-H, Huang Y-S, Chiu P-W, Krasheninnikov A V. and Suenaga K 2015 Single-Layer ReS_2: Two-Dimensional Semiconductor with Tunable In-Plane Anisotropy *ACS Nano* **9** 11249–57

[49] Krishnamurthi S and Brocks G 2020 Spin/charge density waves at the boundaries of transition metal dichalcogenides *Phys. Rev. B* **102** 161106